# Elucidating and Mitigating High-Voltage Degradation Cascades in Cobalt-Free LiNiO<sub>2</sub> Lithium-Ion Battery Cathodes

Kyu-Young Park, Yizhou Zhu, Carlos G. Torres-Castanedo, Hee Joon Jung, Norman S. Luu, Ozge Kahvecioglu, Yiseul Yoo, Jung-Woo T. Seo, Julia R. Downing, Hee-Dae Lim, Michael J. Bedzyk, Christopher Wolverton, and Mark C. Hersam\*

LiNiO<sub>2</sub> (LNO) is a promising cathode material for next-generation Li-ion batteries due to its exceptionally high capacity and cobalt-free composition that enables more sustainable and ethical large-scale manufacturing. However, its poor cycle life at high operating voltages over 4.1 V impedes its practical use, thus motivating efforts to elucidate and mitigate LiNiO2 degradation mechanisms at high states of charge. Here, a multiscale exploration of high-voltage degradation cascades associated with oxygen stacking chemistry in cobalt-free LiNiO2, is presented. Lattice oxygen loss is found to play a critical role in the local O3-O1 stacking transition at high states of charge, which subsequently leads to Ni-ion migration and irreversible stacking faults during cycling. This undesirable atomicscale structural evolution accelerates microscale electrochemical creep, cracking, and even bending of layers, ultimately resulting in macroscopic mechanical degradation of LNO particles. By employing a graphene-based hermetic surface coating, oxygen loss is attenuated in LNO at high states of charge, which suppresses the initiation of the degradation cascade and thus substantially improves the high-voltage capacity retention of LNO. Overall, this study provides mechanistic insight into the high-voltage degradation of LNO, which will inform ongoing efforts to employ cobalt-free cathodes in Li-ion battery technology.

#### 1. Introduction

Li-ion batteries (LIBs) have emerged as the dominant rechargeable energy storage technology for portable electronics, electric vehicles, and related mobile technologies.[1] Since LIBs were first commercialized with LiCoO2 (LCO) and graphite, cell-level energy densities have now nearly quadrupled through the incorporation of higher capacity active materials and optimized battery packaging. Nevertheless, demand still exists for even higher energy density LIBs, particularly for electric vehicle applications. For example, the cell-level energy densities of LIBs must approach 350 Wh kg-1 and 750 Wh L-1 for electric vehicles to reach parity with the mileage range of internal combustion vehicles, which implies energy densities of at least 800 Wh kg<sup>-1</sup> and 2600 Wh L-1 from the cathode active materials.<sup>[2]</sup> Furthermore, because cathode

K.-Y. Park, Y. Zhu, C. G. Torres-Castanedo, H. J. Jung, N. S. Luu, J.-W. T. Seo, J. R. Downing, M. J. Bedzyk, C. Wolverton, M. C. Hersam Department of Materials Science and Engineering Northwestern University

Evanston, IL 60208, USA

E-mail: m-hersam@northwestern.edu

K.-Y. Park

Graduate Institute of Ferrous and Energy Materials Technology Pohang University of Science and Technology E-mail: Pohang, Kyungbuk 37673, Republic of Korea

H. J. Jung NUANCE Center

NOANCE Center
Northwestern University
2220 Campus Drive, Evanston, IL 60208, USA
O. Kahvecioglu
Argonne National Laboratory

Applied Materials Division 9700 South Cass Avenue, Lemont, IL 60439, USA

The ORCID identification number(s) for the author(s) of this article can be found under https://doi.org/10.1002/adma.202106402.

DOI: 10.1002/adma.202106402

Y. Yoo, H.-D. Lim

Center for Energy Storage Research

Korea Institute of Science and Technology (KIST)

Hwarang-ro 14-gil 5, Seongbuk-gu, Seoul 02792, Republic of Korea

Y. You

Department of Materials Science and Engineering

Korea University

145, Anam-ro, Seongbuk-gu, Seoul 02841, Republic of Korea

J.-W. T. Seo Volexion, Inc.

4809 North Ravenswood Avenue, Chicago, IL 60640, USA

M. I. Bedzvk

Department of Physics and Astronomy

Northwestern University

Evanston, IL 60208, USA

M. C. Hersam

Department of Chemistry

Northwestern University

Evanston, IL 60208, USA

M. C. Hersan

Department of Electrical and Computer Engineering

Northwestern University

Evanston, IL 60208, USA

1521495, 2022, 3, Downloaded from https://onlinelibary.viely.com/doi/0.1002/datna.20210402 by University Of Chicago Libaray, Wiley Online Library of Conditions (https://onlinelibary.viely.com/terms-and-conditions) on Wiley Online Library for rules of use; OA articles are governed by the applicable Creative Commons License and Conditions (https://onlinelibary.viely.com/terms-and-conditions) on Wiley Online Library for rules of use; OA articles are governed by the applicable Creative Commons License

active materials also play a decisive role in the overall voltage and cost of LIBs,<sup>[3]</sup> considerable effort has been devoted to developing stable and reliable cathode materials with high specific and volumetric energy densities.

The family of layered oxides is the leading LIB cathode material technology due to its stable solid-state intercalation reactions and relatively fast two-dimensional Li-ion diffusion pathways. [4] Specifically, layered oxides of the form LiMO<sub>2</sub> (M = transition metals such as Mn, Co, and Ni) can deliver theoretical capacities approaching 270 mAh g<sup>-1</sup> upon the extraction of one mole of Li. However, the electrochemically reversible capacity typically falls well short of this theoretical limit and is highly dependent on the transition metal component. For instance, the reversible capacity of LCO is only  $\approx$ 160 mAh g<sup>-1</sup> between 3.0 and 4.3 V (all voltages will be expressed with respect to Li<sup>+</sup>/Li.).<sup>[5]</sup> If Ni becomes the majority transition metal component, such as the  $\text{LiNi}_{0.8}\text{Co}_{0.1}\text{Mn}_{0.1}\text{O}_2$  (NCM811) and  $\text{LiNi}_{0.8}\text{Co}_{0.15}\text{Al}_{0.05}\text{O}_2$ (NCA) compositions, then layered oxides can deliver a capacity close to 200 mAh g<sup>-1</sup> within the same potential range. In addition, increasing the operating voltage window to over 4.3 V can extract more Li ions to approach the theoretical capacity limit, but these high-voltage conditions generally lead to severe irreversible degradation.[3,6]

The single-component Ni-based layered oxide LiNiO2 (LNO) is one of the most promising LIB cathode materials because it possesses a capacity close to the theoretical limit ( $\approx$ 240 mAh g<sup>-1</sup>),<sup>[7]</sup> which satisfies the performance criteria for electric vehicles in terms of both specific (≈800 Wh kg<sup>-1</sup>) and volumetric (≈2600 Wh L<sup>-1</sup>) energy densities.<sup>[3]</sup> Moreover, since the Co-free nature of LNO simultaneously addresses the cost and humanrights issues associated with the Co supply chain, [3,8] LNO is regarded as a genuinely sustainable cathode for next-generation LIBs. However, despite its many merits, multiple drawbacks have impeded commercialization of LNO. For example, the production of high-quality LNO requires high precision in its synthetic conditions. Even slight deviations from the synthetic temperature or Ni/Li precursor ratio are highly detrimental to the electrochemical properties of LNO as it deviates from the stoichiometric phase.<sup>[7,9]</sup> While this synthetic problem has been largely resolved with optimized synthetic conditions, [10] a remaining issue for LNO is its poor cyclic stability, especially at the high operating voltages that are required to access its high capacity. In particular, the cycle life of LNO after 100 cycles at 0.5C is less than 75% of the initial capacity of 230 mAh g<sup>-1</sup> when cycled up to 4.3 V. Although cycling to 4.1 V can improve the cyclic retention to 95%, these low-voltage conditions limit the initial capacity to 180 mAh g<sup>-1</sup>.<sup>[6]</sup>

Poor electrochemical stability is commonly observed in layered Ni-rich oxide cathodes when cycled over 4.3 V. The origin of this high-voltage degradation is not caused by a single mechanism, but by a complex entanglement of mechanical and chemical factors. [3,11] Multiphase transitions, [12] large lattice parameter changes, [6] electrochemical creep, [13] and internal fatigue from surface reconstruction [14] can all lead to mechanical cracking and loss of electrical contact to the current collector, ultimately causing capacity fade. These degradation phenomena also compromise secondary particle morphologies that have been widely employed to achieve high tap densities and power densities. [15] In addition, chemical degradation, such as transition metal

dissolution,<sup>[16]</sup> singlet oxygen evolution,<sup>[17]</sup> and Ni-ion migration,<sup>[18]</sup> reduce the surface electrochemical activity,<sup>[19]</sup> and can occur continuously during cycling due to the mechanical damage that generates new surfaces that act as further sites for degradation. In order to increase the stability of Ni-rich layered oxides, mitigation strategies such as secondary particle morphology control<sup>[20]</sup> or doping<sup>[21]</sup> to mitigate internal strain and stabilize particle surfaces have been attempted. Despite these previous efforts, reliably cycling LNO to voltages above 4.3 V, or more broadly, Ni-rich oxides above 4.6 V, remains a challenge largely due to destructive oxygen stacking transitions. Specifically, at low lithium content, LNO or Ni-rich layered oxides undergo an oxygen stacking transition from a face centered cubic (O3) structure to a hexagonal close packed structure (O1) that results in a rapid loss of electrochemical activity.<sup>[22]</sup>

Here, we present a thorough exploration of the high-voltage degradation mechanism of LNO including its relationship to the evolution of oxygen stacking. Due to the loss of lattice oxygen, local oxygen stacking changes from the O3 to the O1 structure occur prematurely in LNO compared to Ni-rich oxides. The subsequent formation of Ni<sub>Ii</sub> defects in the O1 structure then induces irreversible generation of stacking faults that accelerate mechanical degradation in primary particles due to crystal structure incoherency, which rapidly reduce the electrochemical activity of LNO. Since this degradation cascade is initiated by the loss of lattice oxygen, stable high-voltage operation should be achievable through the use of surface coatings that suppress oxygen evolution without compromising other aspects of rechargeable LIB operation. Towards this end, we employ a graphene-based hermetic surface coating that attenuates oxygen loss at high states of charge (SoCs), thus suppressing the initiation of the degradation cascade and substantially improving the high-voltage capacity retention of LNO. Overall, this work provides detailed mechanistic insight into the high-voltage degradation of LNO, resulting in a mitigation strategy that can serve as the basis of next-generation high energy density LIBs.

# 2. Results and Discussion

## 2.1. Oxygen Stacking Transition and Stacking Faults

LNO powder was synthesized with a secondary particle morphology (Figure S1, Supporting Information) by the conventional solid-state method.[10c] Rietveld refinement (Figure S2, Supporting Information) confirmed the high-quality LNO crystal structure with ≈1% Ni<sub>Ii</sub> defect concentration. Upon delithiation,  $\text{Li}_x \text{NiO}_2$  (0  $\leq x \leq$  1) undergoes first-order phase transitions in the order H1, M, H2, and H3 (Figure 1a), where H and M represent the hexagonal and monoclinic phases, resp ectively.[10a,22b,23] As-synthesized LNO begins in the H1 phase, corresponding to an O3-type oxygen stacking with a repeated AB CA BC oxygen sequence (face centered cubic) as shown in Figure 1b (left), where Li and Ni ions occupy octahedral sites coordinated with oxygen ligands. During charging above 4.1 V, O1-type stacking appears with an AB oxygen sequence (hexagonal close packed, Figure 1b, right), which is accompanied by an H3 phase transition. We observed the formation of 5% O1 stacking faults after charging to 4.6 V (Figure S3, Supporting

15214095, 2022, 3, Downloaded from https://onlinelibrary.wiley.com/doi/10.1002/adma.022106402 by University Of Chicago Library, Wiley Online Library on [06/11/2022]. See the Terms and Conditions (https://onlinelibrary.wiley

ons) on Wiley Online Library for rules of use; OA articles are governed by the applicable Creative Commons

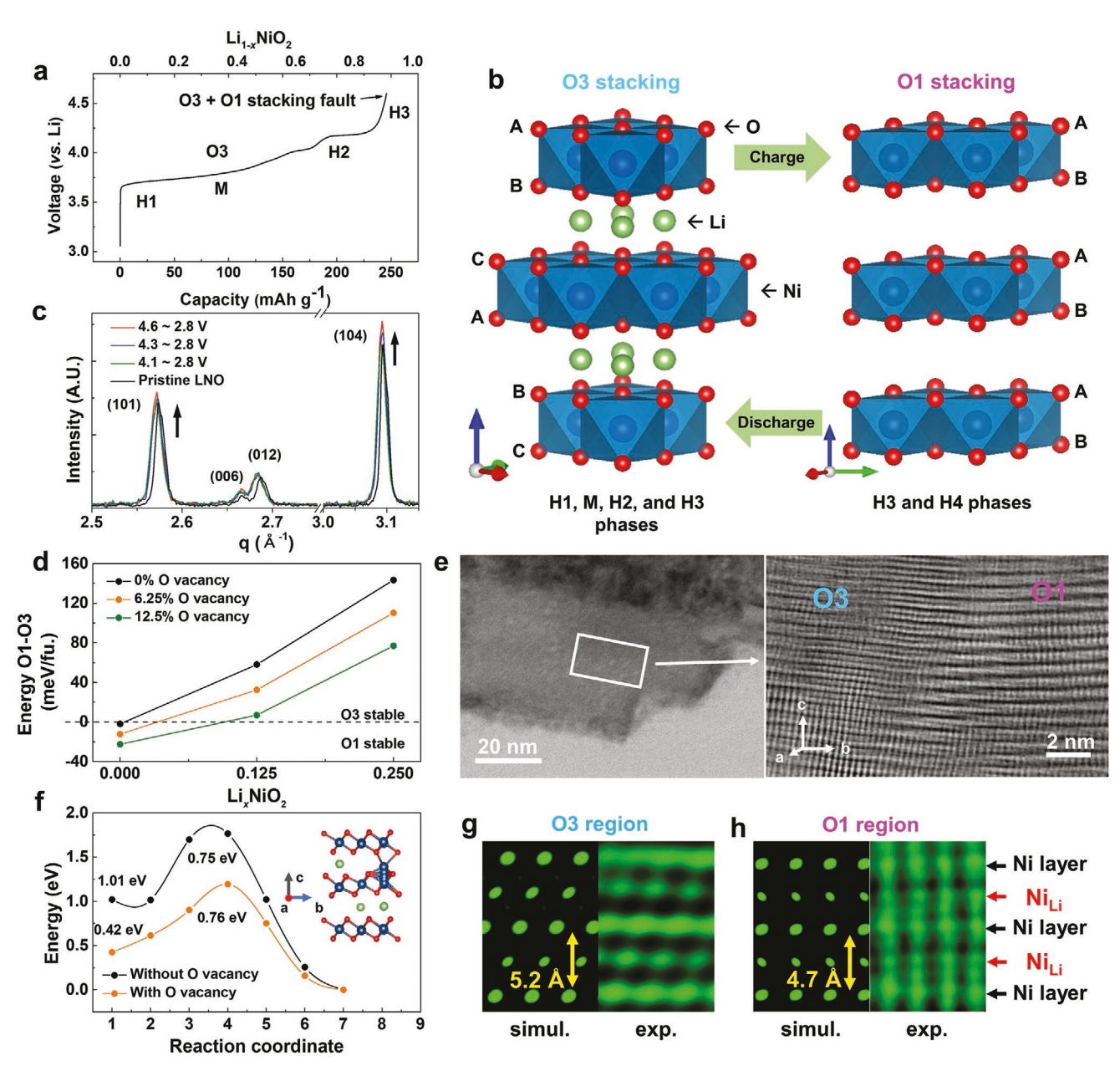


Figure 1. Stacking structural evolution of LiNiO<sub>2</sub>. a) Typical galvanostatic profile of LiNiO<sub>2</sub> and phase transition behavior. b) Atomic models for O3 (left) and O1 (right) stacking. c) X-ray diffraction patterns of pristine LNO electrodes and LNO electrodes after one cycle to 4.1, 4.3, and 4.6 V. d) A stability map of O1 and O3 stackings according to Li content and oxygen vacancy concentration in their crystal lattice. e) TEM images of LNO charged to 4.6 V. f) Activation barrier of Ni ion migration in O1 stacking configurations. Black: without oxygen vacancy; orange: with oxygen vacancy. Observation of Ni ion arrangements in g) O3 and h) O1 stacking configurations was made possible by RABF; right-inset figures show the simulation results of O1 and O3 stackings with Ni defects.

Information), which is consistent with previous literature.<sup>[24]</sup> Although it has been reported that sustained high-voltage conditions for more than 20 h results in additional H'3 (defective H3 with mainly O3 stacking) and H4 (mainly O1 stacking) phases, these phases are rarely observed in conventional galvanostatic charging and discharging.<sup>[24,25]</sup>

In principle, the electrochemically induced O1 stacking can reversibly glide back to the original O3 stacking during relithiation. [26] However, our X-ray diffraction (XRD) results show that the partial O1 stacking (i.e., O1 stacking faults) remain

even after complete relithiation. Specifically, Figure 1c shows the XRD patterns of LNO electrodes after one cycle to 4.1, 4.3, and 4.6 V cutoff voltages. In these experiments, we hold the voltage at 2.8 V until the current reaches C/50 to confirm that the presence of the stacking faults is not due to kinetic limitations associated with galvanostatic cycling. After subjecting the LNO electrodes to these cycling conditions, the intensities of the (101) and (104) peaks increase with increasing cutoff voltage. Moreover, compared to the XRD pattern of as-synthesized LNO, a noticeable peak broadening is observed for the (h0l) and (0kl)

peaks for the cycled electrodes (more details of the XRD peaks are shown in Figure S4 in the Supporting Information). It is well known that the migration of Ni ions into Li sites results in the simultaneous weakening of the (101) peak intensity and strengthening of the (104) peak intensity. Thus, the observed (104) peak intensity increase can be attributed to the presence of Ni<sub>Li</sub> defects. On the other hand, the increased (101) peak intensity and its abnormal peak broadening are typical diffraction changes caused by oxygen stacking faults along the c-direction. DIFFaX simulation by DIFFaX[27] also supports this conclusion. DIFFaX simulation results for a structure with 5% Ni<sub>Li</sub> defects and  $\approx$ 1% O1 stacking fault concentration provide the best agreement with the experimental results after one galvanostatic cycle, as shown in Figure S5 in the Supporting Information.

#### 2.2. Origin of Stacking Structural Evolution

O1 stacking faults in LNO are generated at high SoCs, which is analogous to the behavior found in LCO. [28] The O3-type structure is thermodynamically stable at low SoCs when compared to the O1-type structure since the O3 stacking configuration has a lower electrostatic energy between NiO2 slabs.[29] However, in the high SoC regime, the reduced c-lattice parameter leads to the overlap of oxygen p orbitals from neighboring NiO2 slabs, which are highly covalent. To minimize the direct interaction between O p orbitals, the oxygen stacking structure transitions into O1-type stacking at high levels of delithiation.<sup>[30]</sup> Despite this qualitative argument, first principles calculations (Figure 1d, black line) show that O3-type stacking is 143 meV/f.u. and 58 meV/f.u. more favorable than the O1-type structure at Li content x = 0.25 and x = 0.125, respectively. Only at a pure NiO<sub>2</sub> composition (Li content x = 0) does the O1-type structure become 2 meV/f.u. more favorable than the O3-type structure.<sup>[29]</sup> These calculations thus suggest that the O1-type structure should only appear at nearly full delithiated compositions of LNO (≈270 mAh g<sup>-1</sup> of charge capacity). However, our experimental observations consistently reveal that O1 stacking faults form much earlier near a  $\text{Li}_{\approx 0.1} \text{NiO}_2$  composition (≈240 mAh g<sup>-1</sup>, Figure S3, Supporting Information), which is concomitant with the H3 phase transition.<sup>[24]</sup>

This apparent inconsistency between the theoretical and experimental phase diagrams can be resolved when considering the effect of lattice oxygen loss. Oxygen evolution during electrochemical cycling is a common issue in layered oxide cathode materials.[3,17] In particular, Ni-rich layered oxides lose oxygen from the surface following charging to ≈4.1 V, triggering electrochemical instability at high voltages.[12] We investigated the relationship between oxygen evolution and high SoCs by calculating the oxygen defect formation energy of LixNiO2 for O1-type and O3-type structures at different Li concentrations: x = 0.25, 0.125, 0 (Figure S6, Supporting Information). The oxygen vacancy formation energies for O3-Li<sub>x</sub>NiO<sub>2</sub> E(O3-O<sub>vac</sub>) at x = 0.25, 0.125, and 0 are 1.79, 1.16, and 0.36 eV, respectively. In comparison, the oxygen vacancy formation energies for O1-Li<sub>x</sub>NiO<sub>2</sub>  $E(O1-O_{vac})$  at x = 0.25, 0.125, and 0 are 1.59, 0.65, and -0.30 eV, respectively. Both O3-type and O1-type structures show lower oxygen vacancy defect formation energies as Li content decreases, suggesting that oxygen loss is favorable at high SoCs. Specifically, the oxygen defect formation energy in O1-NiO<sub>2</sub> is negative, which implies that oxygen vacancy formation in this structure is highly favorable and could go beyond the dilute limit. In contrast, the oxygen vacancy defect formation energy in O3-NiO<sub>2</sub> remains positive even when fully delithiated, suggesting that the O3-type structure can better retain oxygen in the lattice during charging. Therefore, maintaining O3-type stacking is critical to suppressing oxygen loss and improving the long-term cycling performance of LNO.

The interplay between oxygen vacancy formation and O3–O1 stacking changes leads to a deleterious positive feedback loop. We compared the energy difference between O1-type and O3-type structures with 6.25% (orange) and 12.5% (green) oxygen vacancies (Figure 1d) and found that the O1-type structure becomes stable earlier during charging when oxygen vacancies are present. In other words, oxygen vacancy formation drives an earlier transition from O3-type to O1-type stacking, while the formed O1-type stacking facilitates the formation of oxygen vacancies. This self-reinforcing synergistic effect explains why O1-type stacking, when formed under high voltage charging, is highly detrimental to the material structure as it leads to irreversible oxygen loss and ultimately capacity fade

Oxygen vacancy formation and gas release mainly occurs at the liquid-solid (i.e., electrolyte-active material) interface rather than at solid-solid interfaces (e.g., grain boundaries). [31] Consequently, the local oxygen vacancy concentration near the exterior surface of a secondary particle is likely to be higher than near the interior, which suggests that the O3-O1 stacking transition should be observed locally near the surface. Figure 1e shows scanning transmission electron microscopy (STEM) images of the LNO surface when charged to 4.6 V. Most of the LNO particle surface has already transformed into a NiOlike phase (Figure S7, Supporting Information), but the nearsurface region still maintains a layered structure (Figure 1e). We observed a significant amount of O1 stacking in the surface region although the overall percentage of O1 stacking is expected to be  $\approx 5\%$ , [30] corroborating the spatial favorability of O1 stacking transitions near the surface. Moreover, this result is in line with recent observations that the bulk structure of LNO cycled to 4.3 V has the O3 structure, [18] whereas the surface of LNO possesses the O1 structure after 100 cycles.<sup>[6]</sup>

Besides leading to earlier O3-O1 stacking transitions, Ni migration easily occurs in O1-type stacking, forming Ni<sub>Li</sub> antisite defects. First principles calculations show that the thermodynamic driving force for Ni ions to move into the Li layer is 0.42 and 1.01 eV with and without oxygen vacancies, respectively, with a migration barrier of ≈0.75 eV (Figure 1f; Figure S8, Supporting Information). Direct observation by reverse annular bright-field (RABF)<sup>[32]</sup> STEM on LNO charged to 4.6 V confirms the Ni<sub>Li</sub> defect formation as shown in Figure 1g. In the O3 structure region, Ni ions are arranged diagonally with Ni<sub>Li</sub> defects, which is a well-known transition metal atomic configuration for O3-type layered oxides (see the inset simulation result). On the other hand, Ni ions are arranged in a line exactly along the caxis in the O1 stacking region (Figure 1h). Moreover, additional Ni ions between layers are observed. This configuration agrees well with the simulation results for Ni<sub>I,i</sub> defects in the O1-type

15214095, 2022, 3, Downloaded from https://onlinelibrary.wiley.com/doi/10.1002/adma.022106402 by University Of Chicago Library, Wiley Online Library on [06/11/2022]. See the Terms and Conditions (https://onlinelibrary.wiley.

conditions) on Wiley Online Library for rules of use; OA articles are governed by the applicable Creative Commons

structure (right inset of Figure 1g,h with the simulation details provided in Figures S9 and S10 in the Supporting Information). Additional Ni ions between the  $\mathrm{Ni}_{\mathrm{Li}}$  and  $\mathrm{NiO}_2$  layer are expected due to the severe distortion of the structure.

Impurities between slabs affect the stacking sliding dynamics. Specifically, the  $Ni_{Li}$  defect plays a role as a "pillar" between  $NiO_2$  layers, impeding the oxygen stacking gliding between O1 and O3. For example, the H4 phase is expected to have a  $CdI_2$  structure with pure O1 stacking, but actual oxygen stacking contains a considerable amount of O3 stacking faults due to its site-exchanged  $Ni_{Li}$  defects in the original O3 structure. [22b,24] If the as-synthesized O3-type LNO has a  $Ni_{Li}$  concentration of more than 7%, the stacking transition into O1-type is completely blocked during charging by the maximized pillar effect. [25] Likewise,  $Ni_{Li}$  defects in O1 stacking contribute to the formation of O1 stacking faults during cycling by reducing the stacking transition reversibility back to O3.

#### 2.3. High-Voltage Degradation of LiNiO2

In general, the oxygen stacking transition is a detrimental structural evolution that can induce creep and cracking of active particles, as observed not only in many LIB layered cathode materials

but also sodium-ion cathode materials. [26,33] Especially for LNO, the substantial c-lattice parameter change accompanying the H2-H3 two-phase reaction accelerates the generation of local stacking faults and induces significant mechanical degradation. Figure 2a shows the typical intergranular cracks found in a secondary particle of LNO after 50 cycles up to 4.3 V at a C/10 rate with substantial primary particle creep observed by scanning electron microscopy (SEM). This primary particle creep becomes more significant following 4.6 V cycling (Figure S11, Supporting Information), which is consistent with recent literature.<sup>[13]</sup> Cross-sectional TEM of the surface region shows that serious bending occurs at the edge of layers (red arrows in Figure 2b) and that the deformation is quite different from previously observed straight cracks along (003) planes (see the white arrows in Figure 2b).[13] The atomic-scale view of the particle edge (Figure 2c) shows that this unexpected bending is attributed to the incoherency of the oxygen stacking structure. The O3 and rock salt phases share the same oxygen framework of AB CA BC stacking, [34] but the O1 structure possess a different AB stacking sequence (Figure S12, Supporting Information). Once the O1 stacking faults are formed between O3 stacking (bulk) and rock-salt (surface) phases along the (003) plane as shown in the inset figures of Figure 2c, dislocations are inevitably formed (yellow-colored inset figure and Figures S13 and S14

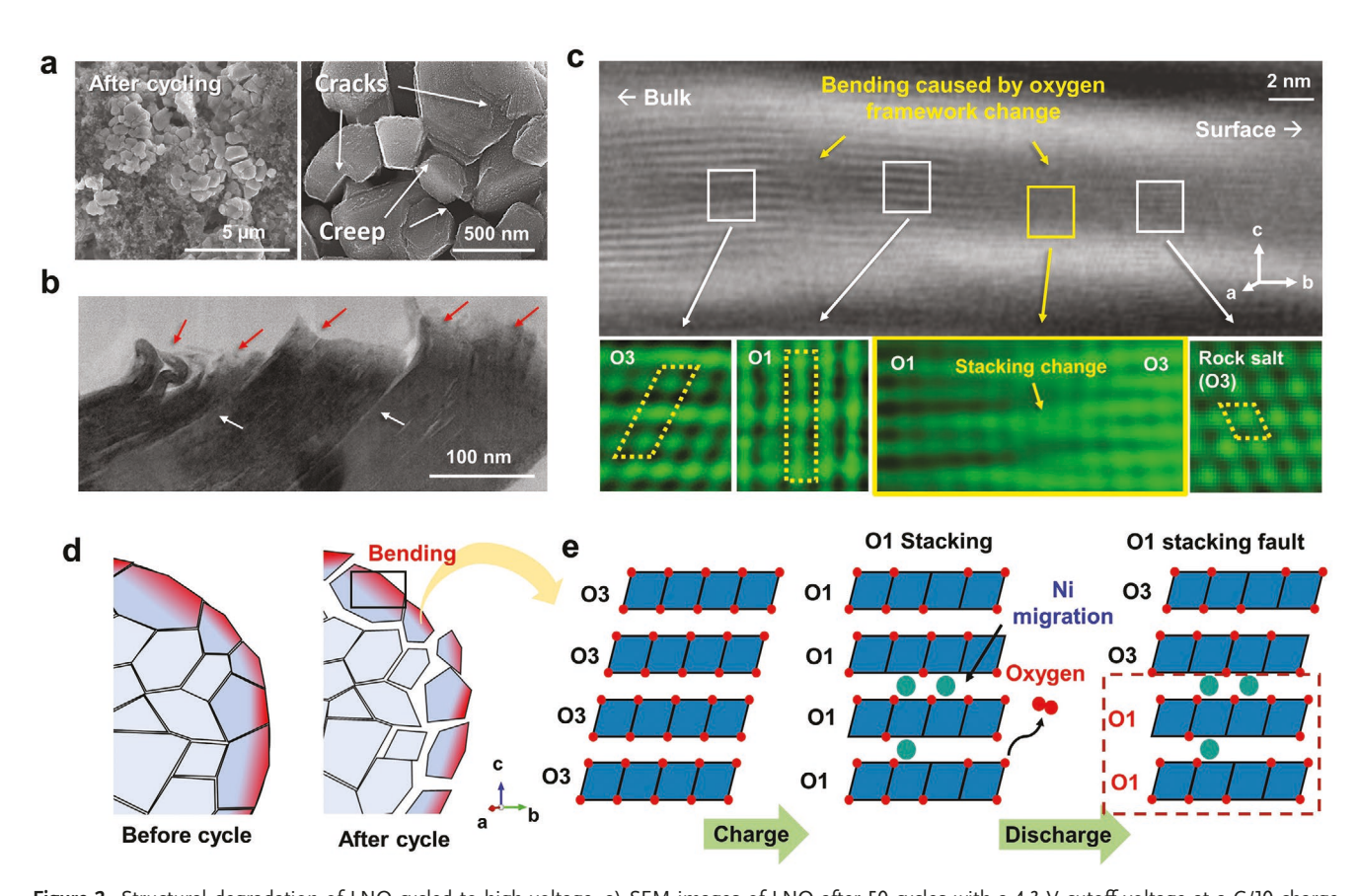


Figure 2. Structural degradation of LNO cycled to high voltage. a) SEM images of LNO after 50 cycles with a 4.3 V cutoff voltage at a C/10 charge rate. In the magnified images, cracking and creep are observed in primary particles. b) Cross-sectional TEM image of LNO charged to 4.6 V. Bending (red arrows) and cracks (white arrows) along the (003) plane are observed. c) High-resolution TEM and its local RABF images for the bending area. d) Scheme for interparticle crack formation caused by primary particle deformation. e) Atomic-scale scheme of the stacking transition and formation of stacking faults.

in the Supporting Information). Thus, severe layer bending occurs, especially at the surface region due to the high concentration of stacking transitions.

Based on these cumulative observations, a cascade for highvoltage degradation of LNO can be delineated. At the initial state, LNO has a pristine secondary particle morphology with O3-type stacking (Figure 2d,e). When the electrode is charged over 4.1 V, loss of lattice oxygen occurs at the secondary particle surface that is in direct contact with the electrolyte (red-colored regions in Figure 2d). As depicted in Figure 2e, the oxygen loss provides a thermodynamic driving force for the O3-O1 stacking transition. The O1 stacking formation facilitates further oxygen vacancy formation and detrimental structural evolution. Following the O3-O1 stacking transition, Ni migration occurs in the local O1 stacking region. These Ni<sub>1i</sub> antisite defects act as pillars between NiO2 slabs, which prevent the slabs from gliding back during discharge, causing the stacking change to be irreversible. Thus, the O1 stacking faults are increasingly prevalent and result in incoherency of the oxygen framework. After repeated cycles, the accumulated stacking faults and oxygen evolution accelerate the primary particle deformation of bending, creep, and cracking, especially for the red region in Figure 2d. Eventually, the primary particle deformation leads to interparticle cracking within the secondary particles, resulting in compromised internal electrical connections after cycling as depicted in Figure 2d (right).

#### 2.4. Mitigation of High-Voltage Degradation

In light of the high-voltage degradation cascade, the key to realizing high-voltage operation of LNO is to suppress the initial surface oxygen loss and thus the O1 stacking transition following charging. Moreover, the suppression of oxygen evolution should also alleviate associated issues such as chemomechanical degradation or electrolyte decomposition.<sup>[17,35]</sup> To test this hypothesis, we prepared LNO powders possessing small secondary particle sizes (≈3 µm, Figure S1, Supporting Information) to maximize the surface area. We then conformally coated these particles with a hermetic layer to suppress the release of oxygen. In particular, we selected a graphene exterior coating because of its established ability to suppress oxygen evolution from layered cathode materials.<sup>[36]</sup> In addition, since graphene coatings primarily interact with underlying surfaces via weak van der Waals forces, we can decouple the effects of oxygen evolution suppression from changes in the surface oxygen coordination that occurs with other coatings such as Al<sub>2</sub>O<sub>3</sub>.<sup>[37]</sup>

Figure 3a shows the galvanostatic profiles of bare LNO (black) and ≈1 wt% graphene-coated LNO (red, G-LNO). The inset SEM image shows that coating the LNO particles with graphene using a Pickering emulsion method<sup>[38]</sup> yields a surface coating with high conformality (additional SEM images are provided in Figure S15 in the Supporting Information). An abnormal overpotential exceeding 4.1 V, corresponding to the H2-H3 phase transition region, is observed in the G-LNO profile. The dQ/dV graph and cyclic voltammetry (Figure 3b) also exhibit this electrochemical response change. Except for the initial overshooting in Figure 3a (corresponding to the initial anodic overshooting between 3.6 and 3.8 V) due to the

coating,[36] other phase transition regions having O3 stacking were not affected by the presence of graphene. This observation supports the conclusion that the H2-H3 phase transition over 4.1 V, which typically releases oxygen gas and initiates the O1 stacking transition, is affected by the exterior coating. In situ differential electrochemical mass spectrometry (DEMS) directly confirmed that the graphene coating significantly suppresses oxygen gas evolution at high potentials. As shown in Figure 3c, the bare-LNO electrode releases oxygen gas above 4.1 V and then carbon dioxide over 4.4 V due to electrolyte decomposition,[17,18] whereas the G-LNO electrode shows no detectable release of oxygen gas and significantly reduced amount of evolved carbon dioxide. Additional experiments on thermally initiated oxygen evolution and X-ray photoelectron spectroscopy characterization of the surface Ni oxidation state further support the anti-gassing function of the graphene coating (Figures S16 and S17, Supporting Information).

To directly compare the structural stacking change associated with oxygen gas evolution, we used high-resolution synchrotron XRD to assess bare-LNO (black) and G-LNO (red) electrodes after one and ten cycles between 2.8 and 4.6 V. Figure 3d (top) shows the XRD patterns of the bare-LNO and G-LNO electrodes after one cycle. Compared to bare-LNO, the G-LNO electrode exhibited narrower (h0l) peak broadening. Moreover, the intensities of the (101) and (104) peaks are relatively low in the G-LNO electrode, suggesting that the stacking structural evolution is mitigated by suppressed oxygen gas evolution. After ten cycles, the bare-LNO electrode showed serious XRD peak broadening due to accumulated stacking faults and loss of crystallinity (Figure 3d, bottom). In contrast, the G-LNO electrode still maintains its high-quality crystal structure with well-defined XRD peaks (more details of the XRD peaks are provided in Figures S18 and S19 in the Supporting Information). Further comparison of the structural change before gas evolution (≈4.1 V, H2 phase) showed identical XRD patterns for both electrodes as shown in Figure S20 in the Supporting Information, but the XRD patterns of the H3 phase (4.6 V) exhibited reduced O1 stacking transition for the G-LNO electrode (Figure S21, Supporting Information).

The suppression of the O1 stacking transition enables a significantly improved cycle life of LNO as shown in Figure 3e,f. Specifically, the G-LNO electrode maintains 95% capacity retention after 50 cycles at C/10 at 4.3 V, whereas bare-LNO only retained 50% of the initial discharge capacity for the same level of cycling. Moreover, the G-LNO electrode showed a 77% capacity retention even at 4.6 V cutoff, whereas bare-LNO exhibited poor capacity retention close to 35% for the same cycling conditions. SEM images of Figure 3g show that the secondary particle morphology of G-LNO remained intact unlike bare-LNO (Figure 2a) after 50 cycles at 4.3 V. After removing the coated graphene from the surface, we confirmed that the extent of creep and cracking in the primary particles is significantly reduced because the exterior coating suppressed the O1 stacking structural evolution (Figure 3g, bottom, with more SEM images provided in Figures S11, S22, and S23 in the Supporting Information).

We further enhanced the cycle life by introducing larger LNO particles (over 15  $\mu$ m) with the exterior graphene coating to minimize the lattice oxygen loss (denoted as LG-LNO, see

15214095, 2022, 3, Downloaded from https://onlinelibrary.wiley.com/doi/10.1002/adma.202106402 by University Of Chicago Library, Wiley Online Library on [06/11/2022]. See the Terms and Conditions (https://onlinelibrary.wiley.com/doi/10.1002/adma.202106402 by University Of Chicago Library, Wiley Online Library on [06/11/2022]. See the Terms and Conditions (https://onlinelibrary.wiley.com/doi/10.1002/adma.202106402 by University Of Chicago Library, Wiley Online Library on [06/11/2022]. See the Terms and Conditions (https://onlinelibrary.wiley.com/doi/10.1002/adma.202106402 by University Of Chicago Library, Wiley Online Library on [06/11/2022]. See the Terms and Conditions (https://onlinelibrary.wiley.com/doi/10.1002/adma.202106402 by University Of Chicago Library.wiley.com/doi/10.1002/adma.202106402 by University Of Chicago Library.wiley.com/doi/1

inditions) on Wiley Online Library for rules of use; OA articles are governed by the applicable Creative Commons

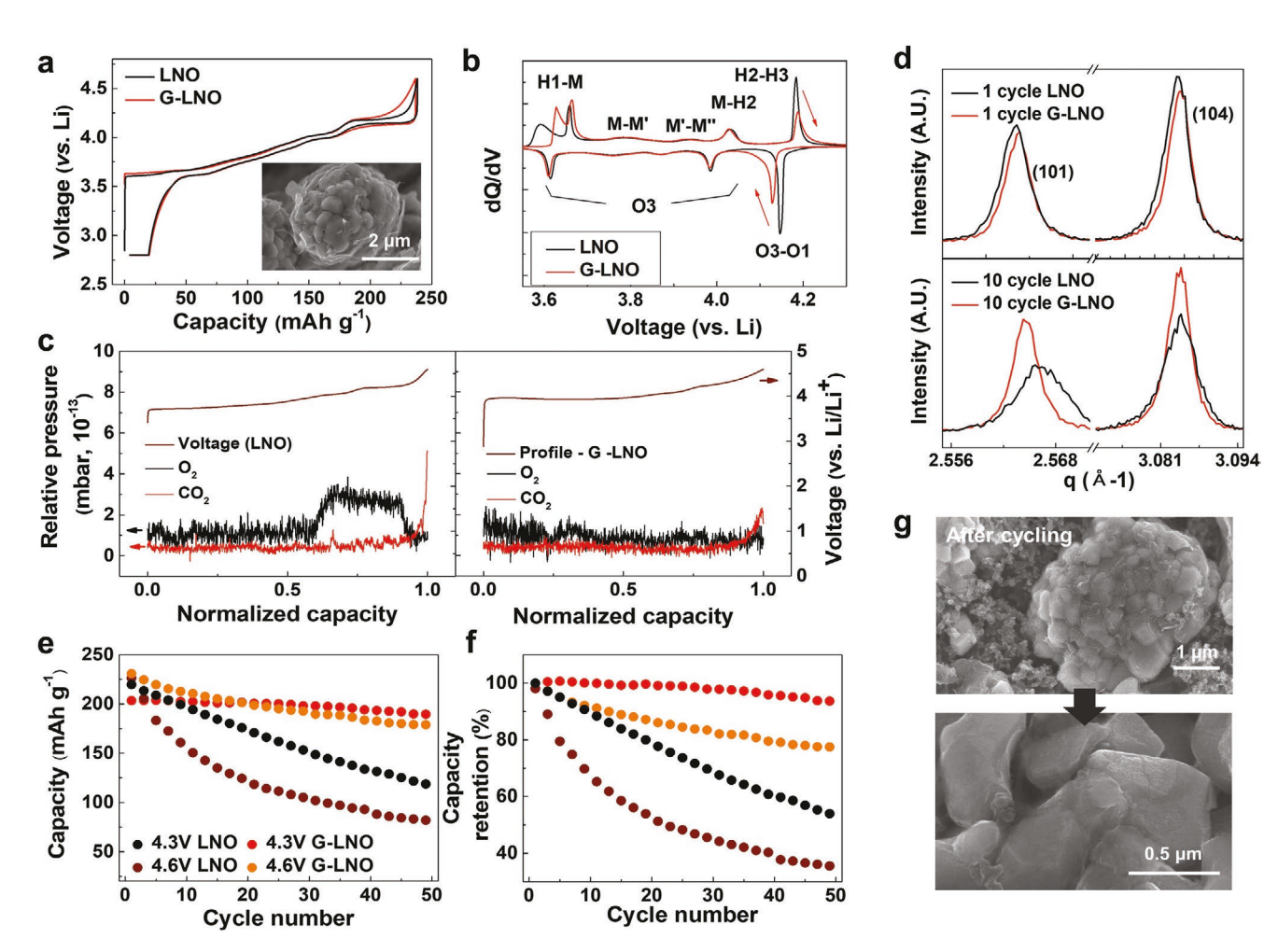


Figure 3. Electrochemical characteristics of LNO with suppressed oxygen evolution. a) Galvanostatic charge/discharge profiles of bare LNO (black) and graphene-coated G-LNO (red) with SEM image (inset). b) Differential capacity versus voltage curves for bare LNO (black) and G-LNO (red). c) In situ DEMS results of (left) bare LNO and (right) G-LNO. Red and black lines indicate the relative pressure of CO<sub>2</sub> and O<sub>2</sub> gases, respectively. d) High-resolution powder XRD results of 1 cycle (top) and 10 cycles (bottom) for bare LNO (black) and G-LNO (red) electrodes. e) Discharge capacity versus cycle number for LNO and G-LNO at 4.3 and 4.6 V cutoff at C/10. After lithiation, the cells were held at 2.8 V until C/50 to minimize kinetic effects. f) Discharge capacity retention versus cycle number. g) SEM images after cycling of (top) LNO particle and (bottom) inside primary particles. In these images, the graphene coating was removed, and the area underneath was observed.

Figure S24 in the Supporting Information). As shown in Figure S25 in the Supporting Information, LG-LNO outperforms the electrochemical stability and rate capability at 4.3 V compared to G-LNO because the increase in the particle size reduces the overall area of the electrolyte-bulk interface, [31] further mitigating lattice oxygen loss. Figure 4a,b shows the cycle life performance at 1C with 4.3 and 4.6 V cutoff voltages, respectively, for control bare-LNO (black) and LG-LNO (red) electrodes. The control electrode maintained only about 40% capacity retention after 100 cycles at 4.3 V, whereas LG-LNO showed a substantial improvement in capacity retention up to 85% under the same cycling conditions (Figure 4a). After 100 cycles with a 4.6 V cutoff voltage, the LG-LNO electrodes continued to deliver an improved capacity retention of 76% compared to 53% retention for the control electrode. It should be noted that all electrodes show relatively rapid capacity degradation in the early stages of cycling, which likely results from secondary particles being cracked by c-lattice parameter changes associated with the H2-H3 phase transition at higher current densities (Figure S26, Supporting Information). Further investigation of the cyclic retention was tested in a graphite full-cell configuration with 4.5 V cutoff voltage. As shown in Figure 4c, the capacity retention of LG-LNO was 74% while the control electrode showed 55% capacity retention after 100 cycles. After 500 cycles, despite the high cutoff voltage, the capacity of LG-LNO was maintained at over 56%, while the capacity of the control electrode had dropped to only 35% (more full-cell results are provided in Figure S27 in the Supporting Information). Therefore, under all testing conditions, the LG-LNO electrodes show a substantial improvement in cycling stability, which can be attributed to the high-voltage degradation cascade being arrested by the hermetic graphene coating suppressing oxygen evolution.

#### 3. Conclusion

Increasing the Ni content in layered oxide cathodes improves the energy density and reduces the cost of LIBs, but also leads to www.advancedsciencenews.com

www.advmat.de

15214095, 2022, 3, Downloaded from https://onlinelibrary.wiley.com/doi/10.1002/adma.202106402 by University Of Chicago Library, Wiley Online Library on [0611/2022]. See the Terms

ons) on Wiley Online Library for rules of use; OA articles are governed by the applicable Creative Commons Licens

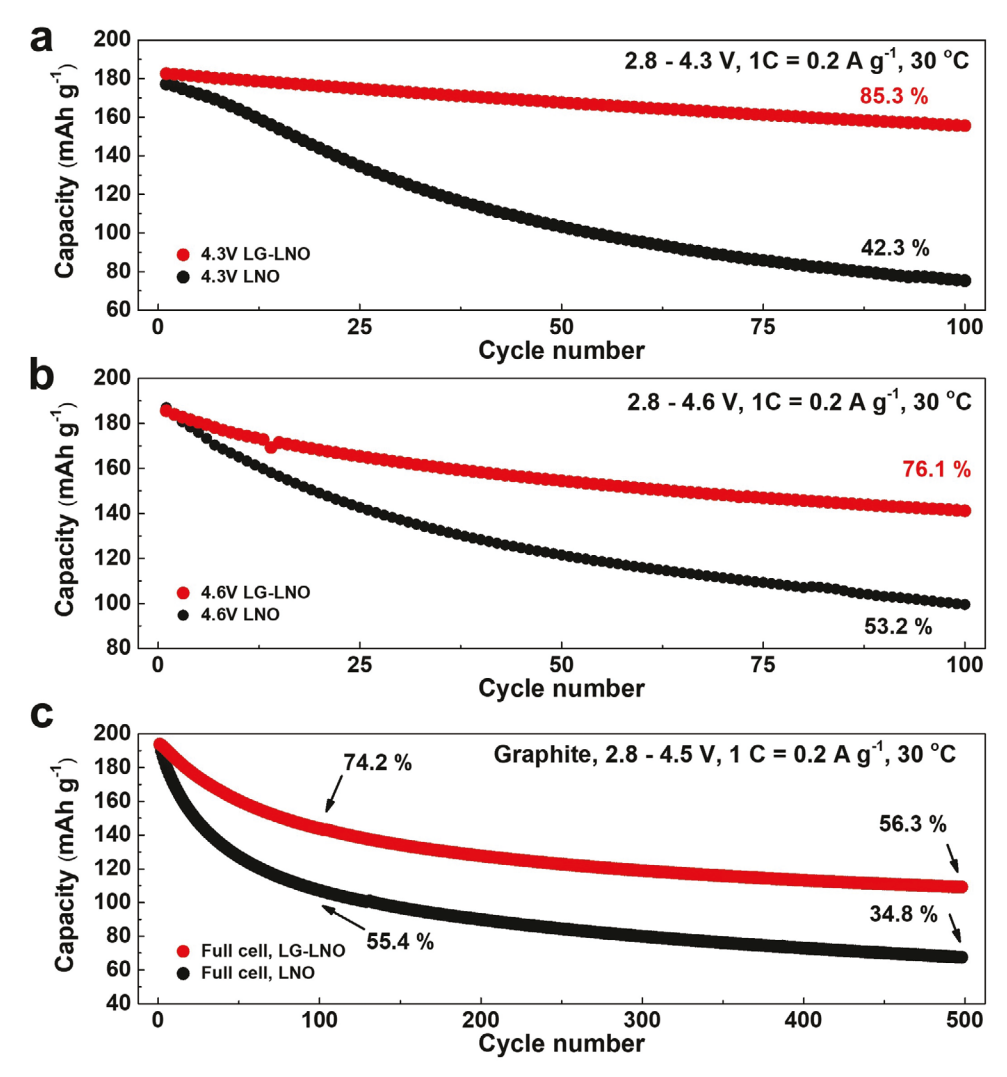
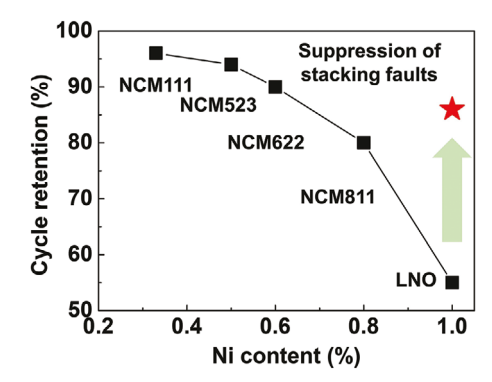


Figure 4. Long-term cycling characteristic of surface-stabilized LNO. Discharge capacity versus cycle number for LNO (black) and LG-LNO (red) at a rate of 1C with a) 4.3 and b) 4.6 V cutoff voltages. c) Full-cell cycling test at a rate of 1C for a 2.8–4.5 V voltage window.

compromised electrochemical cycle life. LiNiO2 is the ultimate goal of high-Ni-content layered oxide cathodes with exceptionally high specific and volumetric energy densities in addition to more sustainable and ethical large-scale manufacturing. Nevertheless, the realization of the high-voltage operation of LNO is fundamentally challenging since the single-component Ni composition results in earlier detrimental oxygen stacking changes compared to multicomponent layered oxides, ultimately leading to the lowest cycle retention (Figure 5). In this study, we have identified that lattice oxygen loss and the O1 stacking transition are the main reasons for the irreversible capacity loss of LNO when charged to the high-voltage region (up to 4.6 V). Moreover, the appearance of Ni<sub>Li</sub> defects in the O1 structure diminishes the reversibility of oxygen gliding, resulting in irreversible stacking faults. These stacking structural changes then accelerate mechanical degradation, such as creep, cracking, and even bending of the layered structure due to incoherency of the oxygen framework, causing rapid capacity fade. Consequently,



**Figure 5.** Overcoming the traditional tradeoff between Ni content and cycle retention. A map of the relationship between Ni content and cycle retention for Ni-rich layered oxide cathodes. NCMxyz indicates  $\text{LiNi}_{0.x}\text{Co}_{0,y}\text{Mn}_{0.z}\text{O}_2$  except for NCM111 (NCM111 =  $\text{LiNi}_{0.33}\text{Co}_{0.33}\text{Mn}_{0.33}\text{O}_2$ ). This graph represents the capacity retention after 100 cycles with 4.3 V. The black data points are taken from the literature. [44]

15214095, 2022, 3, Downloaded from https://onlinelibrary.wiley.com/doi/10.1002/datna.202104020 by University Of Chicago Library, Wiley Online Library on [06/11/2022]. See the Terms and Conditions (https://onlinelibrary.wiley.

and-conditions) on Wiley Online Library for rules of use; OA articles are governed by the applicable Creative Commons License

suppression of oxygen evolution is the key factor to realizing stable high-voltage operation of LNO. Consistent with this conclusion, conformal exterior graphene coatings that suppress oxygen evolution mitigate changes in oxygen stacking during electrochemical cycling, resulting in substantially improved capacity retention (Figure 5). This detailed mechanistic study thus provides a clear path to enabling high-voltage operation of LNO, which is a key step toward realizing practical high energy density LIBs.

## 4. Experimental Section

Material Synthesis: Ni(OH)<sub>2</sub> precursor powders were synthesized continuously using a Taylor Vortex Reactor (TVR) via the hydroxide co-precipitation method. LiOH·H<sub>2</sub>O (Millipore Sigma) and precursor powder were combined using an acoustic mixer and calcined in a box furnace to obtain LiNiO2 cathode powder. As-synthesized LiNiO2 powder was coated with ≈1 wt% of a graphene nanocomposite using a Pickering emulsion method. The nanocomposite was synthesized by solution-phase shear mixing of graphite (+150 mesh, Millipore Sigma) and ethyl cellulose (4 cP, Millipore Sigma). The ethyl cellulose and shearmixed graphene flake mixture was first sonicated with a mass ratio of 2:1 in acetonitrile solvent. Subsequently, LiNiO2 powder and hexane in a 1:5 v/v ratio of acetonitrile were added to the dispersion. After fractional distillation, the dried composite was heated up to 240 °C for 10 min under an oxygen atmosphere to pyrolyze the residual ethyl cellulose. For a reliable comparison, the bare-LNO powder was also subjected to the same chemical and post-heat treatment procedure as G-LNO. More details on the coating method are described in previously published work.<sup>[38]</sup>

Sample Characterization: XRD measurements were conducted in a Scintag XDS 2000 X-ray diffractometer equipped with a Ge (Li) solidstate detector and a Cu K $\alpha$  anode ( $\lambda$  = 1.5418 Å). The equipment was operated using an accelerating voltage of 40 kV and a current of 20 mA. The synchrotron XRD experiments were carried out at the DND-CAT beamline 5BMC at the Advanced Photon Source at Argonne National Laboratory. The 4.6 V charged samples were sealed in capillaries, which continuously rotated about a horizontal axis to allow a  $2 \times 8 \text{ mm}^2 \text{ X-ray}$ beam to strike the sample along its length. The powder diffractometer was used in a high-resolution Bragg-Brentano geometry with a constant energy of 19.970 keV ( $\lambda = 0.620821$  Å). The incident beam optics setup consists of a double bounce pseudo-channel-cut crystal configuration of two Si(111) crystals. An anti-scatter flight tube followed by Soller slits with a vertical blade for limiting horizontal axial divergence was outfitted on the detector. Additionally, a Ge(220) analyzer crystal was utilized before acquiring the signal with an Oxford Cyberstar scintillation counter. The electron microscope images were obtained by SEM (Hitachi SU8030) and TEM (JEOL ARM 200CF). The simulation setup condition was established using multislice image simulation of Dr. Probe software.[39]

Density Functional Theory Calculations: The density functional theory (DFT) calculations in this work were performed using the Vienna Ab initio Simulation Package (VASP)<sup>[40]</sup> within the projector augmented-wave approach. The projector-augmented wave method was used in conjunction with the Perdew-Burke-Ernzerhof revised  $PBEsol^{[41]}$  version for the exchange-correlation functional. A GGA + U parameterization was used, and the U values for Ni were set to 6.2 eV. Additionally, a cutoff energy of 520 eV for the plane-wave basis set was used, along with  $\Gamma$ -centered k-meshes with a density of 2500 k-points per reciprocal atom in all calculations. The Li ordering of groundstate structures LixNiO2 (no oxygen vacancy or Ni migration) was based on previously reported results.<sup>[42]</sup> The structures with oxygen vacancies were created by fixing the Li ordering and removing nonsymmetric oxygen atoms. To enumerate possible orderings, enumlib<sup>[43]</sup> was employed, and no more than 20 configurations were selected with the lowest electrostatic energy possible as candidate structures. DFT calculations were then executed for these candidate structures,

and the one with the lowest energy was selected as the representative ground-state structure. All calculations were spin-polarized with the spin states designated to be ferromagnetic. For the nudged elastic band (NEB) calculation of Ni migration, the Li ordering was first reordered based on the structure with an out-of-plane Ni atom migration. The same ordering method used for creating the structure with oxygen vacancies was applied. Finally, Li ordering was fixed and a path was created for Ni migration.

Electrode Fabrication and Electrochemical Testing: Slurries with active powders, carbon black (MTI corporation, EQ-Lib-SuperP), and PVDF binder (corporation, EQ-Lib-PVDF) with N-methyl-2-pyrrolidone (NMP) were prepared for the electrode fabrication. The mixture was cast on aluminum foil with an active loading density  $\approx 5$  mg cm $^{-2}$  and dried in a 120 °C convection oven. CR2032 coin cells were assembled with Li metal (MTI corporation, reference electrode), glass fiber (Whatman, separator), and 1.2 M LiPF $_6$  in ethylene carbonate/ethyl methyl carbonate of 3:7 volume ratio with 2 wt% of vinylene carbonate (Millipore Sigma, EC/EMC, electrolyte). The full-cell test was conducted with a N/P ratio 1.18 with graphite anode electrode. Coin cells were cycled in an LBT-20084 Arbin battery cycler between 2.8 and 4.3 V or 2.8–4.6 V versus Li/Li $^+$ . The current density of 1C was defined as 200 mA g $^{-1}$ .

In Situ Differential Electrochemical Mass Spectrometry: To analyze gas evolution during cycling, differential electrochemical mass spectrometry (DEMS) was used. The in situ gas analysis system was configured by combining a mass spectrometer (Hiden Analytical HPR-20 R&D) with a potentio-galvanostat (WonA Tech, WBCS 3000). Each cell was assembled into a custom-built coin cell, wherein the cap possessed a small hole (1 mm diameter) in the center to expel gas evolved from the cathode. Each cell was rested for 3 h before the test, and electrochemical performance was measured at a constant rate of 0.1C with a cutoff voltage between 2.8 and 4.6 V. A 20 mg cm<sup>-1</sup> electrode loading density was used to maximize gas detection. During the experiment, the mass flow controller (WIZ-701C-LF) flowed Ar carrier gas at a constant rate of 15 cc min<sup>-1</sup> such that the evolved gas during the electrochemical test was promptly swept into the mass spectrometer.

# **Supporting Information**

Supporting Information is available from the Wiley Online Library or from the author.

# **Acknowledgements**

This work was primarily supported by the Center for Electrochemical Energy Science, an Energy Frontier Research Center funded by the U.S. Department of Energy (DOE), Office of Science, Basic Energy Sciences under Award # DE-AC02-06CH11357. This research was also supported by the Basic Science Research Program of the National Research Foundation of Korea (NRF) funded by the Ministry of Education (Grant No. 2020R1A6A3A03038630). Graphene powder production was supported by the National Science Foundation Scalable Nanomanufacturing Program (Grant Nos. NSF CMMI-1727846 and NSF CMMI-2039268) and the National Science Foundation Future Manufacturing Program (Grant No. NSF CMMI-2037026). This work made use of the EPIC facility of the Northwestern University NUANCE Center, which is supported by the Soft and Hybrid Nanotechnology Experimental (SHyNE) Resource (Grant No. NSF ECCS-1542205), the Materials Research Science and Engineering Center (Grant No. NSF DMR-1720139), the State of Illinois, and Northwestern University. Synchrotron Powder X-ray Diffraction was performed at the DuPont-Northwestern-Dow Collaborative Access Team (DND-CAT) located at Sector 5 of the Advanced Photon Source (APS). DND-CAT was supported by Northwestern University, The Dow Chemical Company, and DuPont de Nemours, Inc. Baseline material synthesis was conducted at the Argonne National Laboratory (ANL) Materials Engineering Research Facility (MERF). MERF was supported

15214095, 2022, 3, Downloaded from https://onlinelibrary.wiley.com/doi/10.1002/datna.202104020 by University Of Chicago Library, Wiley Online Library on [06/11/2022]. See the Terms and Conditions (https://onlinelibrary.wiley.

com/terms-and-conditions) on Wiley Online Library for rules of use; OA articles are governed by the applicable Creative Commons

by the U.S. Department of Energy (DOE), Office of Energy Efficiency and Renewable Energy, and the Vehicle Technologies Office. This research used resources of the Advanced Photon Source, a U.S. Department of Energy (DOE) Office of Science User Facility operated for the DOE Office of Science by Argonne National Laboratory under Contract No. DE-AC02-06CH11357. The authors thank Beam Scientist Mike Guise for his valuable assistance in the beamline during the COVID-19 pandemic. Also, the authors thank DND-CAT Director Denis T. Keane for his support and helpful discussions.

### **Conflict of Interest**

J.-W.T.S. and M.C.H. declare a financial interest in Volexion, Inc., which is a spinout company focused on high-performance LIB cathode materials.

## **Data Availability Statement**

The data that support the findings of this study are available from the corresponding author upon reasonable request.

## **Keywords**

graphene coating, lithium battery, lithium nickel oxide, oxygen evolution, stacking faults

Received: August 15, 2021 Revised: October 16, 2021 Published online: November 19, 2021

- [1] M. Armand, J. M. Tarascon, Nature 2008, 451, 652.
- [2] US DRIVE Electrochemical Energy Storage Technical Team Roadmap, US Council for Automotive Research, Washington, DC 2017.
- [3] W. Li, E. M. Erickson, A. Manthiram, Nat. Energy 2020, 5, 26.
- [4] K. Kang, G. Ceder, Phys. Rev. B 2006, 74, 094105.
- [5] a) Z. Chen, Z. Lu, J. Dahn, J. Electrochem. Soc. 2002, 149, A1604;
   b) K. Mizushima, P. C. Jones, P. J. Wiseman, J. B. Goodenough, Mater. Res. Bull. 1980, 15, 783.
- [6] C. S. Yoon, D.-W. Jun, S.-T. Myung, Y.-K. Sun, ACS Energy Lett. 2017,
- [7] J. R. Dahn, U. von Sacken, C. A. Michal, Solid State Ionics 1990, 44, 87
- [8] C. Banza Lubaba Nkulu, L. Casas, V. Haufroid, T. De Putter, N. D. Saenen, T. Kayembe-Kitenge, P. Musa Obadia, D. Kyanika Wa Mukoma, J.-M. Lunda Ilunga, T. S. Nawrot, O. Luboya Numbi, E. Smolders, B. Nemery, Nat. Sustain. 2018, 1, 495.
- [9] C. Delmas, J. P. Pérès, A. Rougier, A. Demourgues, F. Weill, A. Chadwick, M. Broussely, F. Perton, P. Biensan, P. Willmann, J. Power Sources 1997, 68, 120.
- [10] a) M. Bianchini, F. Fauth, P. Hartmann, T. Brezesinski, J. Janek, J. Mater. Chem. A 2020, 8, 1808; b) J. Xu, F. Lin, D. Nordlund, E. J. Crumlin, F. Wang, J. Bai, M. M. Doeff, W. Tong, Chem. Commun. 2016, 52, 4239; c) H. Li, N. Zhang, J. Li, J. Dahn, J. Electrochem. Soc. 2018, 165, A2985.
- [11] M. Bianchini, M. Roca-Ayats, P. Hartmann, T. Brezesinski, J. Janek, Angew. Chem., Int. Ed. 2019, 58, 10434.
- [12] L. de Biasi, A. Schiele, M. Roca-Ayats, G. Garcia, T. Brezesinski, P. Hartmann, J. Janek, ChemSusChem 2019, 12, 2240.
- [13] Y. Bi, J. Tao, Y. Wu, L. Li, Y. Xu, E. Hu, B. Wu, J. Hu, C. Wang, J.-G. Zhang, Y. Qi, J. Xiao, Science 2020, 370, 1313.

- [14] C. Xu, K. Märker, J. Lee, A. Mahadevegowda, P. J. Reeves, S. J. Day, M. F. Groh, S. P. Emge, C. Ducati, B. L. Mehdi, C. C. Tang, C. P. Grey, Nat. Mater. 2020, 20, 84.
- [15] a) A. O. Kondrakov, A. Schmidt, J. Xu, H. Geßwein, R. Mönig, P. Hartmann, H. Sommer, T. Brezesinski, J. Janek, J. Phys. Chem. C 2017, 121, 3286; b) H.-H. Sun, A. Manthiram, Chem. Mater. 2017, 29, 8486.
- [16] S. H. Song, M. Cho, I. Park, J.-G. Yoo, K.-T. Ko, J. Hong, J. Kim, S.-K. Jung, M. Avdeev, S. Ji, S. Lee, J. Bang, H. Kim, Adv. Energy Mater. 2020, 10, 2000521.
- [17] J. Wandt, A. T. S. Freiberg, A. Ogrodnik, H. A. Gasteiger, *Mater. Today* 2018, 21, 825.
- [18] F. Kong, C. Liang, L. Wang, Y. Zheng, S. Perananthan, R. C. Longo, J. P. Ferraris, M. Kim, K. Cho, Adv. Energy Mater. 2019, 9, 1802586.
- [19] J. Xu, E. Hu, D. Nordlund, A. Mehta, S. N. Ehrlich, X.-Q. Yang, W. Tong, ACS Appl. Mater. Interfaces 2016, 8, 31677.
- [20] H. H. Sun, H.-H. Ryu, U.-H. Kim, J. A. Weeks, A. Heller, Y.-K. Sun, C. B. Mullins, ACS Energy Lett. 2020, 5, 1136.
- [21] a) C. S. Yoon, U.-H. Kim, G.-T. Park, S. J. Kim, K.-H. Kim, J. Kim, Y.-K. Sun, ACS Energy Lett. 2018, 3, 1634; b) C. S. Yoon, M.-J. Choi, D.-W. Jun, Q. Zhang, P. Kaghazchi, K.-H. Kim, Y.-K. Sun, Chem. Mater. 2018, 30, 1808.
- [22] a) J. Yang, Y. Xia, ACS Appl. Mater. Interfaces 2016, 8, 1297;
   b) T. Ohzuku, A. Ueda, M. Nagayama, J. Electrochem. Soc. 1993, 140, 1862.
- [23] C. Delmas, M. Ménétrier, L. Croguennec, S. Levasseur, J. P. Pérès, C. Pouillerie, G. Prado, L. Fournès, F. Weill, *Int. J. Inorg. Mater.* 1999, 1, 11.
- [24] L. Croguennec, C. Pouillerie, C. Delmas, Solid State Ionics 2000, 135, 259.
- [25] J. M. Tarascon, G. Vaughan, Y. Chabre, L. Seguin, M. Anne, P. Strobel, G. Amatucci, J. Solid State Chem. 1999, 147, 410.
- [26] M. D. Radin, J. Alvarado, Y. S. Meng, A. Van der Ven, Nano Lett. 2017, 17, 7789.
- [27] M. M. J. Treacy, J. M. Newsam, M. W. Deem, Proc. R. Soc. A 1991, 433, 499.
- [28] A. Van der Ven, M. K. Aydinol, G. Ceder, J. Electrochem. Soc. 1998,
- [29] M. E. Arroyo y de Dompablo, A. Van der Ven, G. Ceder, Phys. Rev. B 2002, 66, 064112.
- [30] L. Croguennec, C. Pouillerie, A. N. Mansour, C. Delmas, J. Mater. Chem. 2001, 11, 131.
- [31] L. Zou, W. Zhao, H. Jia, J. Zheng, L. Li, D. P. Abraham, G. Chen, J. R. Croy, J.-G. Zhang, C. Wang, Chem. Mater. 2020, 32, 2884.
- [32] D. Kim, H. J. Jung, I. J. Park, B. W. Larson, S. P. Dunfield, C. Xiao, J. Kim, J. Tong, P. Boonmongkolras, S. G. Ji, F. Zhang, S. R. Pae, M. Kim, S. B. Kang, V. Dravid, J. J. Berry, J. Y. Kim, K. Zhu, D. H. Kim, B. Shin, Science 2020, 368, 155.
- [33] J. Alvarado, C. Ma, S. Wang, K. Nguyen, M. Kodur, Y. S. Meng, ACS Appl. Mater. Interfaces 2017, 9, 26518.
- [34] H. Zhang, F. Omenya, P. Yan, L. Luo, M. S. Whittingham, C. Wang, G. Zhou, ACS Energy Lett. 2017, 2, 2607.
- [35] a) S.-K. Jung, H. Gwon, J. Hong, K.-Y. Park, D.-H. Seo, H. Kim, J. Hyun, W. Yang, K. Kang, Adv. Energy Mater. 2014, 4, 1300787;
  b) L. Mu, R. Lin, R. Xu, L. Han, S. Xia, D. Sokaras, J. D. Steiner, T.-C. Weng, D. Nordlund, M. M. Doeff, Y. Liu, K. Zhao, H. L. Xin, F. Lin, Nano Lett. 2018, 18, 3241.
- [36] S. Sharifi-Asl, F. A. Soto, T. Foroozan, M. Asadi, Y. Yuan, R. Deivanayagam, R. Rojaee, B. Song, X. Bi, K. Amine, J. Lu, A. Salehi-khojin, P. B. Balbuena, R. Shahbazian-Yassar, Adv. Funct. Mater. 2019, 29, 1901110.
- [37] T. Cheng, Z. Ma, R. Qian, Y. Wang, Q. Cheng, Y. Lyu, A. Nie, B. Guo, Adv. Funct. Mater. 2021, 31, 2001974.



www.advancedsciencenews.com



www.advmat.de

15214095, 2022, 3, Downloaded from https://onlinelibrary.wiley.com/doi/10.1002/adma.202106402 by University Of Chicago Library, Wiley Online Library on [0611/2022]. See the Terms and Conditions (https://onlinelibrary.wiley.

and-conditions) on Wiley Online Library for rules of use; OA articles are governed by the applicable Creative Commons License

- [38] K.-Y. Park, J.-M. Lim, N. S. Luu, J. R. Downing, S. G. Wallace, L. E. Chaney, H. Yoo, W. J. Hyun, H.-U. Kim, M. C. Hersam, Adv. Energy Mater. 2020, 10, 2001216.
- [39] J. Barthel, Ultramicroscopy 2018, 193, 1.
- [40] G. Kresse, J. Furthmüller, Comput. Mater. Sci. 1996, 6, 15.
- [41] J. P. Perdew, A. Ruzsinszky, G. I. Csonka, O. A. Vydrov, G. E. Scuseria, L. A. Constantin, X. Zhou, K. Burke, *Phys. Rev. Lett.* 2008, 100, 136406.
- [42] H. Das, A. Urban, W. Huang, G. Ceder, Chem. Mater. 2017, 29, 7840.
- [43] G. L. Hart, R. W. Forcade, Phys. Rev. B 2008, 77, 224115.
- [44] H.-J. Noh, S. Youn, C. S. Yoon, Y.-K. Sun, J. Power Sources 2013, 233, 121.